

This item was submitted to [Loughborough's Research Repository](#) by the author.
Items in Figshare are protected by copyright, with all rights reserved, unless otherwise indicated.

Shear band widening mechanism in Ti–6Al–4V under high strain rate deformation

PLEASE CITE THE PUBLISHED VERSION

<https://doi.org/10.1557/jmr.2020.45>

PUBLISHER

Cambridge University Press (CUP)

VERSION

AM (Accepted Manuscript)

PUBLISHER STATEMENT

This article has been published in a revised form in Journal of Materials Research
<https://doi.org/10.1557/jmr.2020.45>. This version is published under a Creative Commons CC-BY-NC-ND. No commercial re-distribution or re-use allowed. Derivative works cannot be distributed. © copyright holder.

LICENCE

CC BY-NC-ND 4.0

REPOSITORY RECORD

Bisht, Anuj, Subhash Kumar, Ka Ho Pang, Rongxin Zhou, Anish Roy, Vadim Silberschmidt, and Satyam Suwas. 2020. "Shear Band Widening Mechanism in Ti–6Al–4V Under High Strain Rate Deformation". Loughborough University. <https://hdl.handle.net/2134/13242476.v1>.

Shear band widening mechanism in Ti–6Al–4V under high strain rate deformation

Anuj Bisht^{1,a)}, Subhash Kumar¹, Ka Ho Pang², Rongxin Zhou², Anish Roy², Vadim V. Silberschmidt², Satyam Suwas¹

¹Department of Materials Engineering, Indian Institute of Science, Bangalore 560012, India

²Wolfson School of Mechanical, Electrical and Manufacturing Engineering, Loughborough University, Loughborough LE11 3TU, U.K.

^{a)}Address all correspondence to this author. e-mail: toninegi01@gmail.com

In this study, mechanical properties and microstructural investigation of Ti64 at high strain rate are studied using a split-Hopkinson pressure bar method under compression for temperatures up to 800 °C. Flow softening in the mechanical response of material to such loading conditions hints at instability in compression, which increases with an increase in temperature. Microstructural characterization of the deformed material is characterized using the electron-backscattered diffraction technique. It reveals the presence of instabilities in Ti64 in the form of a fine network of shear bands. The shear band width grows with an increase in temperature along with the area fraction of shear band in the material, displaying its improved capacity to contain microstructural instabilities at higher temperature. After a detailed microstructural investigation, a mechanism for shear band widening is proposed. Based on this mechanism, a path generating nuclei within shear bands is discussed.

Introduction

Titanium and its alloys are an important class of materials for applications in critical aerospace component [1]. In particular, Ti–6Al–4V (Ti64) is a popular alloy with a big market share. Because of its relevance for industrial applications, extensive studies of mechanical behavior of Ti64 are available in the literature. Its microstructure typically displays Widmanstätten structure consisting of HCP α + BCC β colonies, with the beta titanium phase present in traces at the colony boundaries [2]. It is well known that a deformation microstructure of Ti64 and other Ti alloys below the recrystallization temperature has distinguishable regions of localized strain, with prominent and widespread networks of shear bands [3, 4, 5]. Nucleation of instabilities such as adiabatic shear bands in the microstructure induces localized softening and is a precursor of material's failure by promoting formation and coalescence of voids resulting in crack initiation [6, 7, 8]. Thus, a significant research was done with a focus to study the deformation microstructure, the nature of instabilities, and methods to prevent their formation.

Flow instabilities in Ti64 were classified as “geometric” [3] instabilities as they were found to depend on the stress state.

The microstructure within adiabatic shear bands in titanium is characterized by fine equiaxed grains formed at a high temperature via rotational dynamic recrystallization under dynamic impact/explosive loading conditions [9, 10, 11]. Peirs et al. [12] reported elongated equiaxed grains at the outer edge of shear bands, which became narrower toward the center and eventually breaking down into nanocrystalline grains at their core. Also, Ramesh et al. [13] showed the microstructural evolution caused by a planar dislocation motion and twinning, grouping of dislocations into cells, formation of elongated subgrains along a shear direction, and development of equiaxed nanocrystalline grains. Rittel et al. [14] observed that dynamic recrystallization preceded the shear failure and thus suggested that such failure was an outcome of microstructural evolution leading to localized softening of the material before thermal softening. Shear band formation was also reported to depend on experimental conditions and material parameters. A material with Widmanstätten microstructure was observed to fail at smaller strain than that with the equiaxed microstructure as the crack could easily grow within the laths [4]. An initiation strain for shear band formation showed strain rate dependence, with a lower onset strain at higher strain rates [15]. Shear bands

often display a self-organizing behavior, with a spacing as a function of various parameters that can be modeled using a momentum diffusion and perturbation model framework [16]. Although a shear band is an instability in the microstructure, the value of micro-hardness within the shear band was reported to be higher than that of the surrounding matrix in multiple studies [6, 17].

Shear band formation was also investigated theoretically for plane-strain condition. It was studied by Hutchinson and Tvergaard [18]. They reported that shear bands might form gradually with limited strain localization or localize catastrophically because of initial imperfections in the form of material inhomogeneity. Moreover, the shear band direction was also reported to be more inclined towards the forward direction of material flow. Xing et al. [19] modeled the shear band nucleation from finite-amplitude disturbances (FADs), demonstrating that FADs may coalesce and evolve into a fully developed shear band. Some noteworthy reviews on strain localization and shear band phenomenon were also published [20, 21, 22]. Roy et al. [2, 23] reported that a trace amount of boron to Ti64 delayed the phenomena of strain localization and shear band formation. Molinari et al. [24] investigated adiabatic shear banding under high-speed machining and reported the dependence of shear band width (SBW) and distance between band of cutting speed, and the chip serration was reported to form as a result of thermomechanical instability.

Although many works were focused on formation and microstructure of shear bands, limited studies have focused on the post shear band formation behavior and widening of shear bands. Shear band widening mechanism was studied in nano-scale twin/matrix lamellae Cu–Al alloy and was reported to occur via transformation of the two transition layers into the core shear band region with a detwinned dislocation structure [25]. The primary focus of our study is to investigate the mechanisms of shear band widening in Ti64. Shear band type instabilities form in abundance in Ti64 subjected to compression at a high strain rate and below 900 °C (recrystallization temperature) [5, 26]. Thus, high strain-rate compression tests of Ti64 were performed using a split-Hopkinson pressure bar (SHPB) method for temperatures up to 800 °C to obtain microstructures with shear band instabilities. Mechanical behavior and texture evolution of Ti64 with temperature are analyzed. The obtained deformed microstructure was characterized with an electron-backscattered diffraction technique with a focus on shear bands. Possible shear band widening mechanism during deformation was suggested based on microstructural evidence.

Results

The initial extruded sample was dynamically compressed at various temperatures. The characterization of microstructure

and texture of the dynamically compressed Ti64 demonstrated a predominantly shear-banded microstructure with a strong basal texture along the compression axis. The results for mechanical properties, the evolution of microstructure, and texture after high strain-rate compression are described in detail in the following subsections.

Mechanical properties

The compression test of Ti64 at room temperature (RT), 600 °C, 700 °C, and 800 °C were carried out at a strain rate of 1000 s^{-1} using SHPB; the corresponding compression curves are shown in Fig. 1. The flow stress is considered at strain of 0.05. The magnitude of flow stress and strain to failure are tabulated in Table I. Apparently, the flow stress decreased monotonically with an increase in temperature, whereas the strain to failure increased. The sample compressed at 800 °C did not fail at the end of the test. Initial strain hardening was observed for all the temperatures in compression curves. At RT, the material continuously strain hardened till fracture, although the strain-hardening rate decreased significantly with strain. At the end, the curve dropped and the sample failed instantaneously, indicating fracture because of catastrophic propagation of instability in the microstructure. At 600 and 700 °C, the curves saturated after an initial stage of strain-hardening and became flat. A slight drop in the stress value can be observed in the later part of the curves. By contrast, the sample dynamically compressed at 800 °C showed a continuous gradual decrease in stress after initial stage of hardening. However, the rate of drop in flow stress was not as significant as that observed when recrystallization occurred in the material. Moreover, the gradual drop in flow stress indicated that the softening mechanism other than dynamic recrystallization was initiated during the deformation. The instability and softening behavior were better evident in the strain-hardening plots ($\partial\sigma/\partial\epsilon$ versus σ) presented for the plastic regime of all the samples (Fig. 2). Abrupt dips in the strain hardening are evident even before $\partial\sigma/\partial\epsilon$ value becomes zero. These dips indicate the nucleation of instability in the material in the hardening stage. However, the samples failed only after $\partial\sigma/\partial\epsilon$ became zero. After this, softening was observed in the material as evident from the backward going line with a negative slope. The softening regime of the material was very short at RT and increased with an increase in temperature. It was significant at 800 °C, with a zero value of $\partial\sigma/\partial\epsilon$ followed by a negative one.

Bulk texture evolution

The texture of various samples after compression is represented by inverse pole figure (IPF) shown in Fig. 3(a). The IPF clearly indicates the dominant basal texture along the compression axis as indicated by contours concentrated around the (0001)

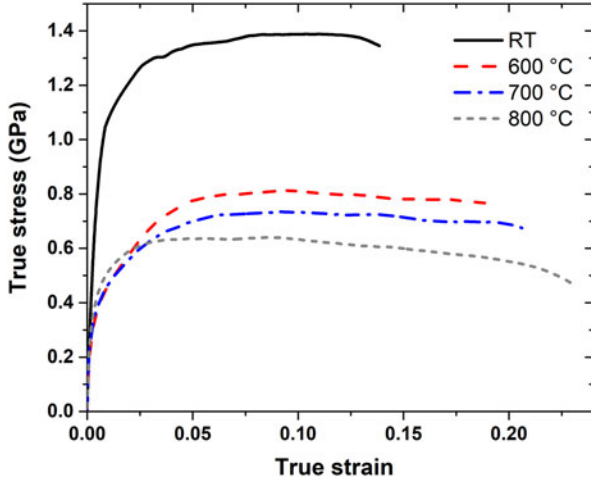


Figure 1: Dynamic compression curves of Ti64 deformed at 1000 s^{-1} for various temperatures.

TABLE I: Flow stress and strain to failure of Ti64 deformed at various temperatures.

Temperature (°C)	Flow stress (GPa)	Failure strain
RT	1.35	0.138
600	0.78	0.191
700	0.69	0.205
800	0.64	0.229 (did not fail)

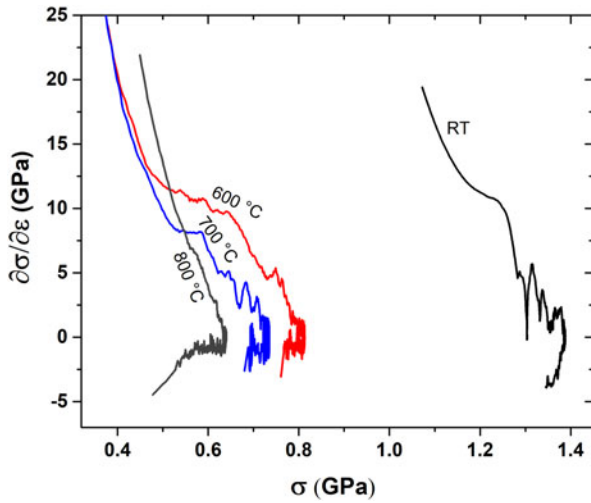


Figure 2: Strain-hardening plot for Ti64 deformed at 1000 s^{-1} for various temperatures.

basal plane. Other texture components were observed, although weak in nature, near $(10\bar{1}1)$ [in Fig. 3(a) RT, 700 °C and 800 °C] and around $(10\bar{1}0)$ [in Fig. 3(a) 700 °C]. The strength of the basal texture first increased with the deformation temperature up to 700 °C and thereafter decreased for 800 °C. The same trend was also exhibited by the texture index (TI), which is the indicator of the overall texture strength

of the material. Its variation with deformation temperature [Fig. 3(b)] suggested that the basal texture was the dominant texture component, governing the bulk texture of the material.

Microstructural evolution

The microstructure of the material was investigated at the mid-region on the transverse section of the compressed sample (site A in Fig. 4). The IPF map superimposed with the image quality (IQ) for the initial and compressed samples is shown in Fig. 5. The IPF shows the local crystal orientations as decoded by the colored IPF triangle. The plane orientation shown in the IPF maps corresponds to the orientation as seen from compression direction (CD). The IQ map is the map of signal quality captured at each point, and it reveals deformation features like slip lines, shear bands, and twin traces. The initial material shows grains in a colony structure, with a beta titanium phase present in trace amounts at the colony boundaries, typical for a Ti64 alloy [2].

The sample compressed at RT is shown in Fig. 5(b). As the sample was fractured, the electron back-scattered diffraction (EBSD) scan was recorded at site A below the fracture surface. In the region investigated, developed shear bands were not observed. However, there were dark traces along the bands [bottom left area in Fig. 5(b)] indicating strain localization. At 600 °C [Fig. 5(c)] and 700 °C [Fig. 5(d)], the microstructure shows an abundance of basal grains and multiple sharp shear bands of varying thickness, criss-crossing each other and forming a network. Such a network structure of adiabatic shear bands was reported for Ti64 at a high strain rate [27]. Although grains were predominantly reoriented to the basal orientation, there were other, non-reoriented grains, displaying resistance to reorientation. Few such grains also show resistance to shear band propagation. By contrast, the sample deformed at 800 °C [Fig. 5(e)] at site A demonstrated shear banding in most parts of the region; both fine and thick shear bands were found. It can be observed that the SBW increased from the top to the bottom of the scan, as evident in Fig. 5(e). To confirm that a large unindexed region in Fig. 5(e) was due to shear band and not an artefact caused by poor polishing, an additional EBSD scan [Fig. 5(f)] was recorded at site B adjacent to site A (see Fig. 4) in the same polished sample. The microstructure at site B was properly indexed, providing the confidence in the data recorded at site A for the sample deformed at 800 °C. The shear bands observed at site B had a higher number density, were closely spaced, and more diffused than the ones observed for 600 °C [Fig. 5(c)] and 700 °C [Fig. 5(d)] samples. However, the area fraction of shear bands at site A [Fig. 5(e)] was higher than that at site B [Fig. 5(f)]. It is interesting to note that the fraction of grains with basal orientation was relatively low at 800 °C when compared to 600 and 700 °C.

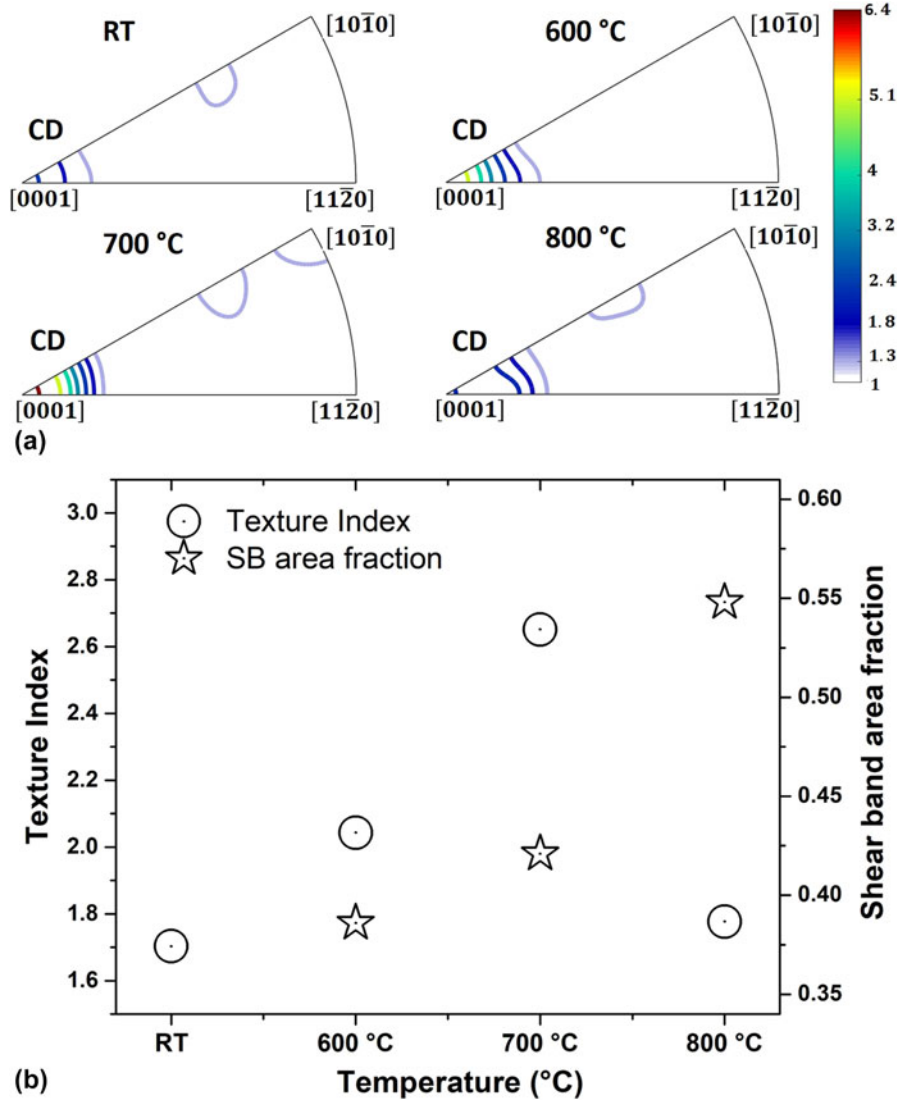


Figure 3: (a) Inverse pole figure along CD of deformed samples depicting texture evolution. (b) Plot showing texture index and shear band area fraction as function of deformation temperature.

Shear bands are a prominent feature observed in this investigation. Thus, it is important to quantify the parameter related to them. Their width is a bulk parameter associated with shear bands. The distribution of SBW observed in samples dynamically compressed at different temperatures is shown in Fig. 6. At 600 °C, the average SBW was about 2 μm , and the corresponding distribution is narrow. With increase in temperature, the distribution broadened, and there was a shift to higher magnitudes, indicating an increase in the mean SBW. It should be noted that the shift in peak decreases with an increase in temperature and is not very discernible for 700 and 800 °C. Nonetheless, thicker SBs are present at 800 °C than that at 700 °C and can be seen as the extended tail of the distribution at 800 °C (Fig. 6). This was accompanied by a decrease in the frequency of narrower SBs resulting in a reduction in peak height at 800 °C. The increase in SBW

with temperature was accompanied by an overall increase in the SB area fraction [Fig. 3(b)]. The SB distribution in the region investigated at site A had SBs with width as high as 35 μm .

On a close inspection, many interesting features associated with SB were found when the data from all the samples were considered together. The magnified IQ map of selected sections from various samples demonstrating these features are shown in Fig. 7. First, many intersections of independent shear bands, with high angles of intersection ($>45^\circ$), resulting in an irregular criss-cross pattern, are evident. The second interesting feature observed in the microstructure is the bifurcation/branching of individual SBs as indicated by arrows in Figs. 7(a)–7(c). It is interesting to note that in such branches usually one of them (in whole or in segment) has a low angle with respect to the horizontal direction (perpendicular to the

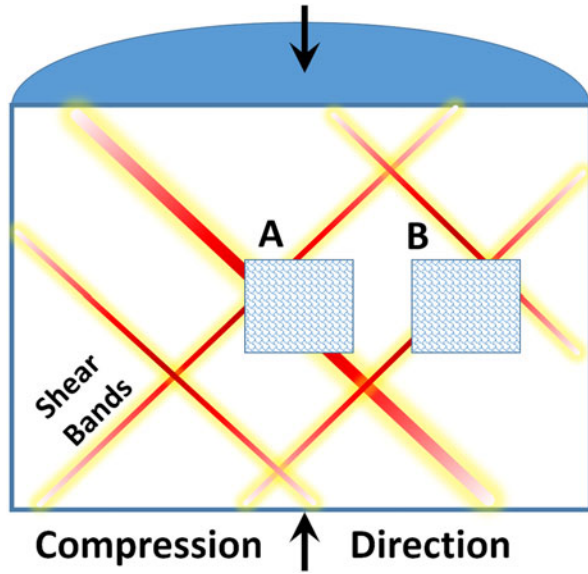


Figure 4: Schematic showing the regions of investigation (A and B) in the mid-section of compressed sample.

CD). Additionally, few individual SBs without any branching were also observed to have a very low angle with respect to horizontal direction, and some segments were almost horizontal. Such observations deviate from our understanding of SBs, according to which they are expected to be aligned along the direction of the maximum macroscopic shear stress ($\sim 45^\circ$). Even taking the anisotropic nature of crystal into account, resulting in SB direction different from that of the maximum macroscopic shear stress, the presence of segments of nearly horizontal SB cannot be explained. Lastly, many small grains of various sizes and shapes were observed and indexed within the SBs in the region marked inside ovals in Fig. 7 and indicated by arrows in Fig. 8. They were found in many shapes, ranging from globular/equiaxed (with the aspect ratio close to 1) to rectangular (with low aspect ratios) indicated by arrows in Fig. 8(a). These grains are important as they can act as nuclei for static/dynamic recrystallization under appropriate conditions. Such nuclei are in abundance, especially at the junctions of intersections of multiple SBs. They are absent, or rarely observed in SBs of smaller width. Table II shows the number of nuclei with temperature within SBs. For a conservative estimate, only fine grains of size between 1 and 2 μm , and which are present within the SB region, are considered as nuclei. The data indicate that the number of nuclei increases with temperature. Observing the trend in SBW and the number of nuclei, it can be said that the number of nuclei within the SBs increases as the width of SB increases. The nuclei were observed to have orientation both similar to that of the neighboring grains and deviating from the neighboring grains (Fig. 5), with the former being prevalent.

The shear band cuts the grains and divided the material into regions (Fig. 5). Zhou et al. [28] reported that the

boundary condition influenced considerably the shear band formation, including both patterns and numbers of SB. Moreover, strain localization because of shear band formation can in-turn significantly alter the local mechanical response of Ti64. Thus, the process of SB formation in the material is expected to initiate the changes in local boundary conditions of grains adjacent to SBs. The modification in the local boundary condition should manifest as change in slip activity around the shear band region. To probe these minute changes, grain reference orientation deviation (GROD) axis plot is shown in Fig. 8 for selected regions. This plot shows the distribution map of the misorientation axis with respect to a reference orientation in the grain. In the studied case, the point in the grain with the minimum kernel average misorientation (KAM) was considered as reference orientation. Qualitative information related to slip system(s) can be deduced from the GROD axis plot. Two interesting trends were observed based on the GROD axis map. First, the misorientation axis was different across the shear band, as deduced from different colors in the GROD plots [regions inside the ovals in Figs. 8(a) and 8(b)]. Nonetheless, at many places, it was also found to be similar across the shear band. Second, on the same side of the shear band, a misorientation axis change was evident with distance (in a direction perpendicular to SB) away from the region adjacent to the SB. Point-to-point and point-to-origin misorientation line profile [Fig. 8(c)] along line LL, which cross a SB and is marked in Fig. 8(b), shows a greater misorientation built-up adjacent to SB than compared with the region away from it. This further displays the activity change adjacent and away from SB. This is consistent along the length of the shear band, indicating the change in the slip activity in the region adjacent to it.

Discussion

The temperature has a significant effect on mechanical behavior and texture of the studied material. The main findings related to the shear band evolution and the widening mechanism are discussed below in detail.

Effect of temperature on mechanical properties and texture

Instability formation and flow localization are the active deformation mechanism in Ti64 in the high temperature and high strain rate regime adopted in this study [5]. During deformation of Ti64, the α (HCP) phase undergoes a rigid-body rotation to reorient the α colony to a favorable orientation for basal and prismatic slips, that is, α grains with basal planes aligned along the CD resulting in the observed basal texture. After considerable strain, the deformation in the favorably orientated region can become restricted, leading to flow localization and shear band initiation. In essence, the kinked

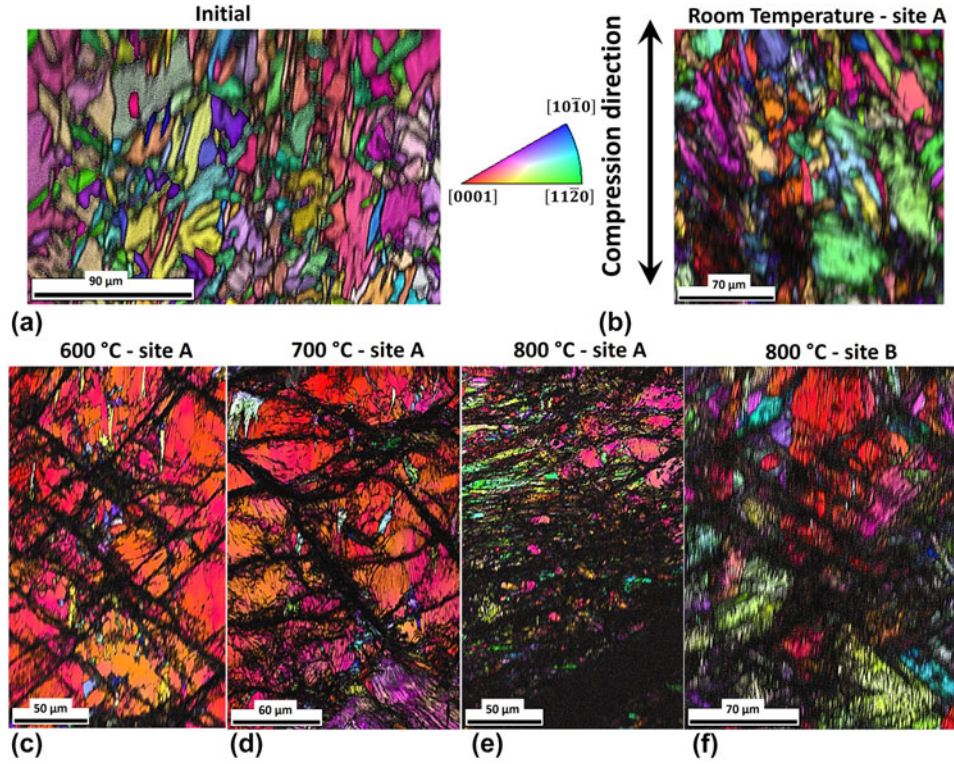


Figure 5: Inverse pole figure map superimposed with image quality (IQ) for Ti64 compressed at 1000 s^{-1} strain rate at different temperatures. Site A and site B designates the region in the sample investigated.

α colony in later stages of deformation can lead to a localized shear band [29]. Kinking and SBs are instabilities in the deformed material. Formation of such instabilities reflects as flow softening of the material in the stress-strain curve. At a lower temperature, the localization and SB formation resulted in abrupt failure of the compressed material. The localization event was distinctively observed as a dip in the strain hardening plot (Fig. 2). With increase in temperature, the dips were low and more frequent, indicating increased incidents of instability formation in the material. Nevertheless, such instabilities had relatively lower effect, as the material's capacity to contain instability improved with temperature, although at a price of a reduced flow stress. With improved ductility, a high fraction of α grains were reoriented to the basal orientation with strain, and the texture strength increased with temperature. At 800°C , the pyramidal slip also became active, and, thus, the basal orientation was no more the only favorable orientation for slip. Even in iodide titanium, the propensity of twinning decreases and that of prism and pyramidal slip increases with an increase in temperature [30]. This was manifested as weakening of the texture at 800°C .

Shear band evolution

Effect of temperature on shear band

The shear bands were localized at the region of fracture and absent in the nearby region as observed in the RT compression,

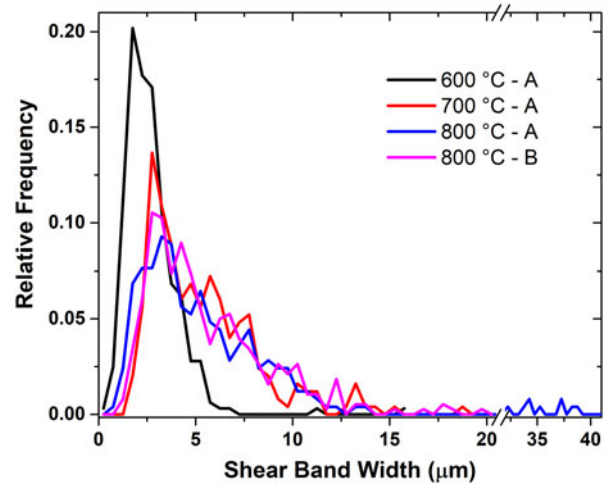


Figure 6: Shear band width distribution in Ti64 compressed at different temperatures.

whereas shear bands were present in significant numbers and spread over the sample when deformed at 800°C (Fig. 5). Moreover, the average SBW in the material increased, and its distribution broadened with temperature. Thus, it can be said that with an increase in temperature, the distribution of shear band tends to homogenize in the deformation volume. This is primarily because of the more uniform distribution of strain with temperature. Hence, the phenomenon of strain localization

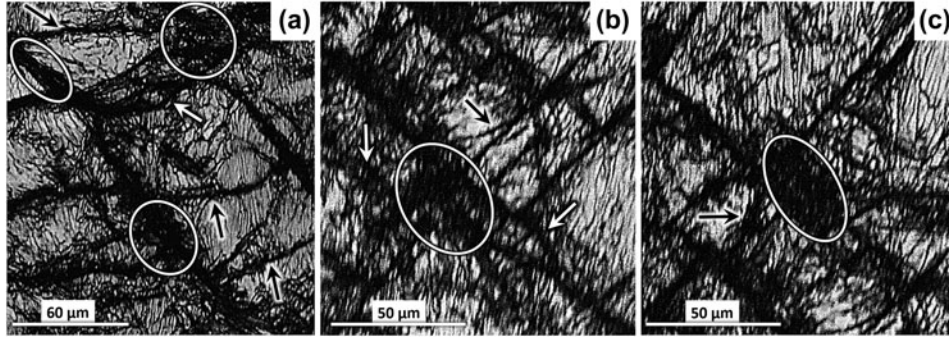


Figure 7: Image quality map of selected regions showing features of shear bands observed in various samples. Region (a) corresponds to 700 °C sample, whereas (b) and (c) corresponds to 600 °C sample.

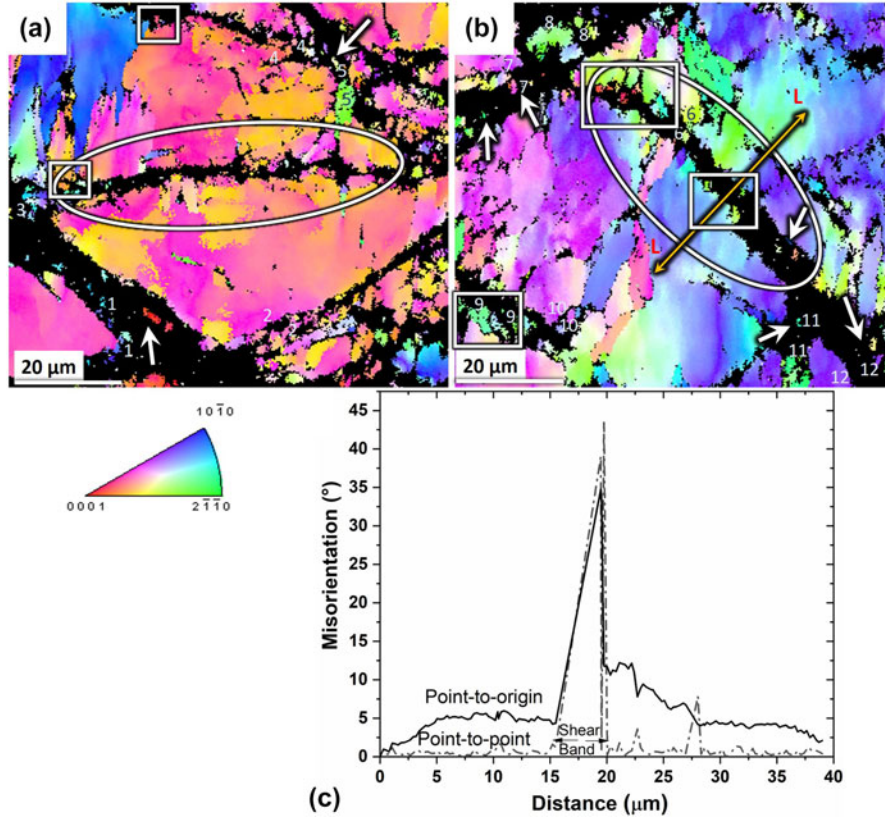


Figure 8: (a, b) Grain reference orientation deviation axis plots for selected areas from 700 °C sample showing difference in the axis of GROD across shear band. The misorientation axis can be decoded using the colored IPF triangle. (c) Point-to-point and point-to-origin misorientation line profile along line LL marked in (b).

was no more limited to the center of the deformed sample, and shear bands could nucleate more homogeneously in it.

The maximum width of the shear band that the material can contain increases with temperature. Thus, it can be said that the capacity of the material to incorporate instability (shear band) and its resistance to failure improves with temperature. As mentioned above, the improvement in the shear band containing capacity of the material results in its improved ductility. At present, the reason for the increase in the material's capacity to contain shear bands with temperature

is not clear. Generally, a SB is a region of high disorder, with atoms deviating from their equilibrium lattice positions. It is thus expected that the atoms in the shear-banded region have a lower coordination number and a relatively higher atomic volume than atoms in the crystalline phase. This, in one view point, is the reason for an unstable nature of SBs. With temperature, atoms in the crystalline phase of the material become more disordered and their atomic volume grows because of the increase in the amplitude of atomic vibrations. Currently, it can only be speculated that the improvement in

TABLE II: Number of nuclei observed within SB. Only grains between size 1 and 2 μm have been considered as nuclei.

Temperature ($^{\circ}\text{C}$)	Nuclei
RT	4
600	65
700	78
800	196

the shear band containing capacity with temperature is related to the reduction in the difference in atomic state (atomic volume and coordination number) of atoms in the base crystalline material and atoms within shear bands. The improved stability of shear band can also be considered from another perspective. The presence of SBs in the material results in a discontinuity at the grain–SB interface in a previously continuous region. SBs are generally defined as a region with concentrated accumulated strain resulting in the material's inability to contain shear stresses and, thus, in some way demonstrate fluid type characteristics. Because of the viscous flow of material in SBs, the boundary of the grain adjacent to the shear band is under high frictional shear stress. The resulting change in the boundary condition due to the shearing effect promotes a change in the slip activity in the region adjacent to the SB (zone of shear) when compared with the region far away, as observed by the change in the GROD axis across SB (Fig. 8). This is also evident from the misorientation line profile in Fig. 8(c). With an increase in temperature, the material's flowability rises, thanks to a larger number of slip systems. As a result, the zone of shear is expected to broaden with temperature, with the concentrated shear stress at grain–SB boundaries relaxing. Thus, the propensity of instability created in the material due to the presence of SB reduces.

Shear band widening mechanism

From the frequency distribution of SBW (Fig. 6), it is apparent that the mean SBW increased with temperature. At 600 $^{\circ}\text{C}$, the SB distribution was very narrow. It should be noted that the strain achieved by material at the end of the compression test also increased with temperature. It can be said that thin SBs were nucleated in the material, growing/widening with deformation (strain increase). The microstructural mechanism for the widening of SBs was not investigated in the literature. The microstructural investigation in this study was done after compression. Nonetheless, the microstructural evidence (Figs. 7 and 8) for various samples revealed different features of SB development. Assuming that the mechanism of microstructural deformation remained similar in the compression regime at various temperatures, a possible mechanism of SB widening and their area increase can be proposed based on our microstructural study. The processes related to the SB

development and widening could be implemented via the following possible routes:

- (i) *Intersecting SBs*: Two independent non-parallel shear bands can intersect each other. The intersection of two (or more) SBs can result in an increased area at the junction. The region at this junction should have a state similar to that within a SB, resulting in an overall increase in the area and the width of SBs at the junction. This is schematically depicted in Fig. 9(a). Regions where the shear band width are observed to increase at the junction are readily evident in Fig. 7.
- (ii) *Branching SBs*: A segment of an individual SB in the microstructure can bend, resulting in deviation in the direction of the SB from the direction of the maximum shear stress. This can happen in the SB segment in the material between two parallel active SBs. The surrounding SBs may have different shearing rates, resulting in a bulk shearing/rotation of the entrapped material including SB segments within it [Figs. 9(b) and 9(c)]. This phenomenon is evident in Fig. 7(a) where the material entrapped between the two sets of parallel SBs with curved SBs, which deviates significantly from the direction of maximum shear stress, are present. The curved nature of SBs reflects the bulk shearing/rotation in the region. A new direction of the SB segment in the macroscopic reference frame deviates from the direction of the maximum shear stress, making it inactive. With further deformation and under the influence of evolving stresses, a new segment of SBs can nucleate at a certain position along the inactive primary SB, with the SB segment starting to deviate from the direction of the maximum shear stress. The new branch of the SB is expected to be along the direction of the maximum shear stress. Now, there are multiple plausible scenarios governed by the deviation of the angle of the inactive SB from the maximum shear stress direction and the nucleation of a new SB branch. The first case is when the new thin SB branch nucleates as soon as the primary SB starts bending. The angle between the new SB branch and the primary SB is small, and the two are nearly parallel. They are approximately aligned along the maximum shear stress direction. In this case, the branch can cut off a small region from the grain and merge back with the primary SB. Such events in repetition can lead to an increase in the SB width as shown in Fig. 9(e). The second case, if there is a delay in the branching of a new SB, the angle between the new SB branch and the primary SB is significant, with the latter deviating considerably from the direction of the

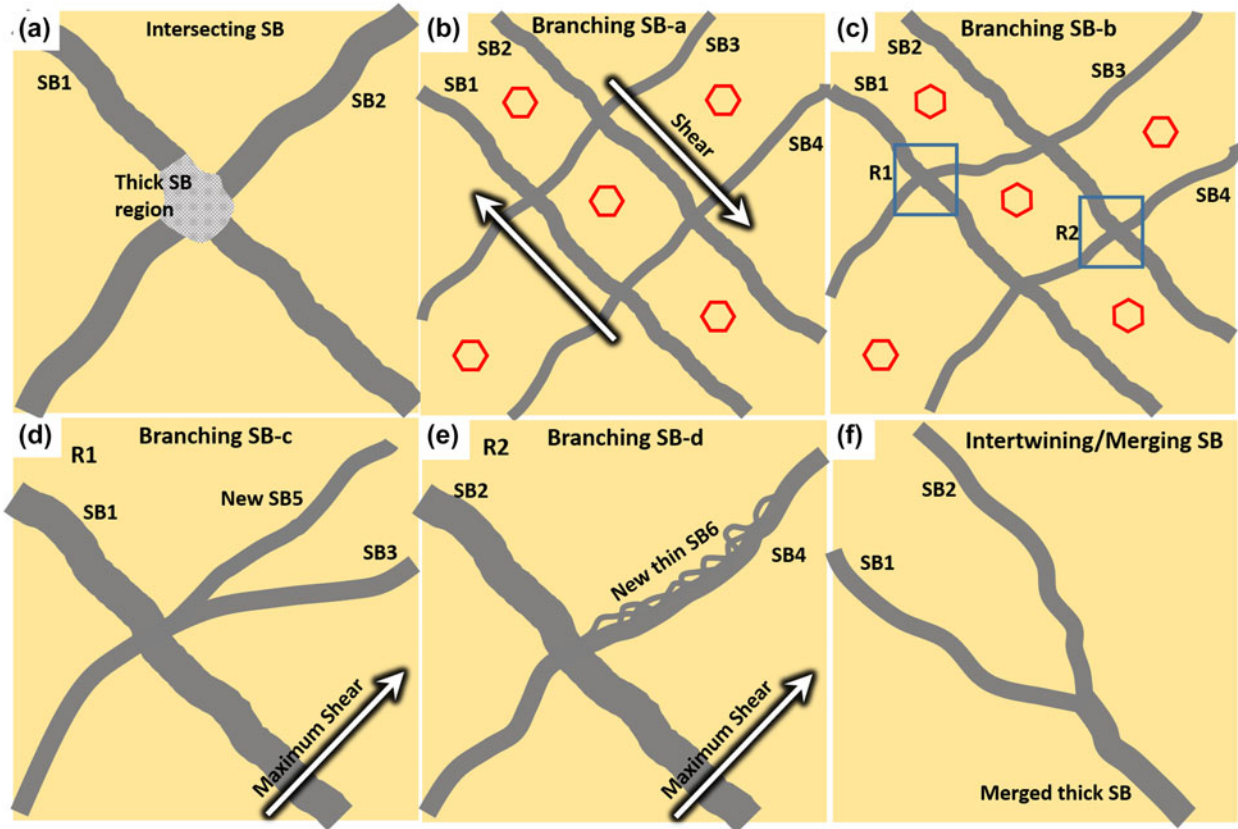


Figure 9: Schematic representation of possible mechanism of SB widening: (a) intersecting SBs; (b–e) branching SBs; and (f) intertwining SBs. Gray: SB. Yellow: Crystalline. Hexagon: local crystal orientation.

maximum shear stress. Thus, merging back by the new SB is not possible. In this scenario, a completely new thick independent branch can form and propagate, resulting in cutting of a part of the grain [Fig. 9(d)]. This grain fragment with continuing deformation can further break into smaller pieces because of high shearing activity of surrounding SBs, effectively resulting in widening of the SB. Such instances of splitting of SB into new branch are clearly evident in the microstructure in Fig. 7 indicated by arrows. Also, notice cases where a branched SB again joins the primary SB (indicated by white arrows in Fig. 7) supporting the discussed mechanism.

- (iii) *Intertwining SBs*: Two parallel independent SBs can bend toward each other and merge, as a result of the activity of grain in their neighborhood. The merger of SBs can result in an increase in their width [shown in Fig. 9(f)]. Although the evidence for this mechanism is not very clear in the microstructure because of our inability to distinguish between SB branching and merging events, it is expected that such a phenomenon is possible and likely operable. This mechanism can be considered as an extension of

discussion and is described for completeness as a possible event.

The processes described above are not mutually exclusive and can operate simultaneously.

Origin of nuclei within shear bands

The number of nuclei within SBs increased with the width of SBs and at junctions as can be observed in Fig. 7. This demonstrates that the nuclei formation is in some sense associated with the SB thickening phenomena. During SB thickening by the mechanism mentioned above, the region entrapped between the shear bands can break down into small fragments forming nuclei within the SB. Moreover, other possible mechanism for nuclei formation within the SB can operate at the grain–SB interface. Caused by slip activity in the grain, slip line ledges can form and protrude into the SB region [Fig. 10(a)]. The ledges protruding into the SB are more prone to erosion because of shear activity of SBs. The ledges (with a very small size) can break from the parent grain into the SB. The ledge can also act as a local crack [Fig. 10(b)], resulting in

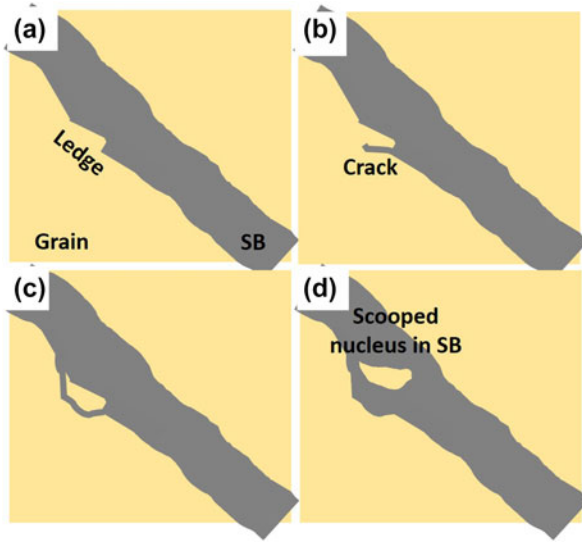


Figure 10: Schematic of steps involved in the “scooping mechanism” of nuclei formation within shear band: (a) Protruding ledge; (b) crack formation at ledge; (c) breakage of a small part of grain and (d) broken part moving within SB as nucleus.

breakage of a small part of the grain that can separate (scoop) and join the SB [Figs. 10(c)–10(d)]. There is evidence of such scooped regions in the SB as observed from the presence of elongated nuclei with low aspect ratios and orientation similar to that of the neighboring grains. Also, there are multiple observable nuclei within the SB, with a similar GROD axis as that of the neighboring grains. Such nuclei–grain pairs are identified by numbers in Fig. 8. The GROD axis is indicative of the slip activity in the region. Thus, similar GROD axes of nuclei–grain pairs indicate that the two regions with a similar slip activity were once connected. Thus, the nuclei could be scooped out from the neighboring grains into the SBs. This mechanism of nuclei formation by removal/erosion of grains into the SB because of shearing activity of SB is termed as “scooping mechanism.” Steps involved in this mechanism are schematically represented in Fig. 10. Regions scooped into the SB can further break down into small pieces because of intense shear activity within the SB. Instances of the grain being scooped into the shear band can be observed in regions enclosed by rectangle in Fig. 8 and supports the “scooping mechanism” of nuclei formation.

Conclusion

High strain-rate compression tests of Ti64 were performed using the SHPB for temperatures up to 800 °C to study the development of shear bands. An onset of instability in the material was observed in stress–strain curve as flow softening and clearly evident as dips in the strain-hardening plot. The

(0001) basal texture developed along the compression axis after deformation, with the texture strength increasing with temperature till 700 °C. By contrast, weakening of the basal texture was found at 800 °C. The microstructure at a high temperature was characterized using EBSD. The presence of instabilities in the microstructure was confirmed and observed in the form of networks of shear bands. The area fraction and the width of the shear bands increased with an increase in deformation temperature, signifying the improved capacity of the material to contain microstructural instabilities at higher temperature. Important features pertaining to SBs including SB intersections/junctions, bent SBs, and SB branches were observed. With this in focus, the possible mechanisms were proposed for SB widening: (i) intersecting SBs, (ii) branching SBs, and (iii) intertwining SBs. Moreover, nuclei were observed within the SBs and in significant numbers at SB junctions. These nuclei can act as a source of recrystallization under appropriate conditions. The event, which could lead to the nuclei formation within the SB, was discussed based on SB activities. After a detailed microstructural investigation, a mechanism for shear band widening was proposed and used to explain the main ways for generation of nuclei within shear bands.

Experimental methods

Initial material and high strain-rate compression

The material in this study is Ti–6Al–4V (Ti64); the as-received material was in a form of a hot extruded rod. The initial material has a colony microstructure with very thin β between parallel α colonies. There are few big grains with unimodal grain size distribution. The area average grain size is 22 μm . The sample for the compression test was extracted from the rod with their compression axis parallel to the extrusion direction. The high strain-rate compression tests of Ti64 at various temperatures were performed using a SHPB. A typical SHPB system consists of a striker bar, an incident bar, a transmission bar, and an absorber at the end to stop the transmission bar. For a RT test, a cylindrical sample with 3 mm diameter and 3 mm length was placed between, and in contact with, the incident and transmission bars. The striker bar was accelerated using a gas gun and made to hit the incident bar. This generated a compressive elastic wave, traveling through the incident bar. The sample was compressed when the wave reached the incident bar and the sample interface. A part of the wave was reflected back into the incident bar, whereas the other part was transmitted through the sample into the transmission bar. Signals of the reflected ($\epsilon_R(t)$) and transmitted ($\epsilon_T(t)$) waves were captured by two strain gauges placed on the incident and the transmission bar. The strain rate $\dot{\epsilon}(t)$, stress $\sigma(t)$, and strain $\epsilon(t)$ experienced by the sample were extracted

from the captured signals based on a one-dimensional elastic-wave theory [31], which gives

$$\dot{\varepsilon}(t) = -\frac{2C}{L} \varepsilon_R(t) \quad , \quad (1)$$

$$\varepsilon(t) = -\frac{2C}{L} \int_0^t \varepsilon_R(t') dt' \quad , \quad (2)$$

$$\sigma(t) = E \frac{A_b}{A} \varepsilon_T(t) \quad , \quad (3)$$

where C is the speed of the elastic wave in the bar, E is the Young's modulus of the bar, A_b is the cross-sectional area of the bars, and A and L are the area and length of sample, respectively.

For the high-temperature test, a resistance furnace was used to heat the sample. Initially, only the sample was heated to the desired temperature in the furnace. After soaking the sample for 10 min at the desired temperature, the incident and transmission bars were brought in contact with the sample seconds before the test. This was done to reduce the temperature drop in the sample before the test and prevent the thermal expansion of the bars during the test.

Texture characterization

The bulk texture measurements were performed with Bruker D8 Discover system using Cu K_α radiation at an accelerating voltage of 40 kV. The measurements were done on the transverse plane of the compressed sample parallel to the CD. Six incomplete pole figures, namely, $\{0002\}$, $\{10\bar{1}0\}$, $\{10\bar{1}1\}$, $\{10\bar{1}2\}$, $\{10\bar{1}3\}$, and $\{11\bar{2}0\}$, were measured experimentally. Complete texture information was calculated from the incomplete pole figure data to obtain an orientation distribution function (ODF). The IPFs were obtained along the compression axis from the ODF. All the calculations and analysis pertaining to texture were carried out using Mtex Matlab code [32].

Microstructure characterization

The microstructural characterization of the initial and compressed states of samples was implemented with the EBSD technique. The compressed samples were sectioned to expose their transverse plane. The EBSD scan was recorded on the mid-section in the transverse plane of the compressed sample (site A) close to the fractured surface. The site A was chosen for the scan as the probability of finding multiple shear bands in this region was high. For selected samples, an additional EBSD scan was recorded at site B, at mid-off center from site A in the transverse section. The positions of the sites in the sectioned compressed sample are depicted schematically in Fig. 4 for clarity.

For EBSD, the samples were prepared by metallurgical route of mechanical polishing followed by electro-polishing. The transverse section of the sample was electro-polished using Struers trade mark A3 electrolyte with a Struers Lectropol-5 (Struers A/s, Stuttgart, Germany) electro-polisher at 36 V. EBSD was performed with a FEI ESEM QUANTA scanning electron microscope (SEM; FEI Company, Hillsboro, Oregon) with an accelerating voltage of 25 kV and a step size of 0.3 μm . The post-processing and analysis of the captured EBSD data are performed using TSL OIM™ analysis software. An IQ signal was primarily used for identification and quantification of shear bands. Qualitative information pertaining to slip system was obtained from GROD axis map.

Acknowledgments

Funding from the Department of Science and Technology (India) through grant number DST/RC-Uk/14-AM/2012 and Engineering and Physical Sciences Research Council (UK) through Grant No. EP/K028316/1 for the project “Modeling of Advanced Materials for Simulation of Transformative Manufacturing Processes (MAST)” is gratefully acknowledged. The authors would also like to thank Dr. Biswaranjan Dash for the help in performing the compression tests and Dr. S. Karthikeyan for permission to use the SHPB in our study.

References

1. J.C. Williams and E.A. Starke: Progress in structural materials for aerospace systems, edited by S. Suresh. *Acta Mater.* **51**, 5775 (2003).
2. S. Roy, A. Sarkar, and S. Suwas: On characterization of deformation microstructure in Boron modified Ti–6Al–4V alloy. *Mater. Sci. Eng., A* **528**, 449 (2010).
3. S.V. Kailas, Y.V.R.K. Prasad, and S.K. Biswas: Flow Instabilities and fracture in Ti–6Al–4V deformed in compression at 298 K to 673 K. *Metall. Mater. Trans. A* **25**, 2173 (1994).
4. A.J. Wagoner Johnson, C.W. Bull, K.S. Kumar, and C.L. Briant: The influence of microstructure and strain rate on the compressive deformation behavior of Ti–6Al–4V. *Metall. Mater. Trans. A* **34**, 295 (2003).
5. S. Roy and S. Suwas: The influence of temperature and strain rate on the deformation response and microstructural evolution during hot compression of a titanium alloy Ti–6Al–4V–0.1B. *J. Alloys Compd.* **548**, 110 (2013).
6. L.E. Murr, A.C. Ramirez, S.M. Gaytan, M.I. Lopez, E.Y. Martinez, D.H. Hernandez, and E. Martinez: Microstructure evolution associated with adiabatic shear bands and shear band failure in ballistic plug formation in Ti–6Al–4V targets. *Mater. Sci. Eng., A* **516**, 205 (2009).

7. **S.P. Timothy and I.M. Hutchings:** Initiation and growth of microfractures along adiabatic shear bands in Ti-6Al-4V. *Mater. Sci. Technol.* **1**, 526 (1985).
8. **Q. Xue, M.A. Meyers, and V.F. Nesterenko:** Self-organization of shear bands in titanium and Ti-6Al-4V alloy. *Acta Mater.* **50**, 575 (2002).
9. **Y. Yang and B.F. Wang:** Dynamic recrystallization in adiabatic shear band in α -titanium. *Mater. Lett.* **60**, 2198 (2006).
10. **L. Kuang, Z. Chen, Y. Jiang, Z. Wang, R. Wang, and C. Liu:** Adiabatic shear behaviors in rolled and annealed pure titanium subjected to dynamic impact loading. *Mater. Sci. Eng., A* **685**, 95 (2017).
11. **Z. Li, B. Wang, S. Zhao, R.Z. Valiev, K.S. Vecchio, and M.A. Meyers:** Dynamic deformation and failure of ultrafine-grained titanium. *Acta Mater.* **125**, 210 (2017).
12. **J. Peirs, W. Tirry, B. Amin-Ahmadi, F. Coghe, P. Verleysen, L. Rabet, D. Schryvers, and J. Degrieck:** Microstructure of adiabatic shear bands in Ti6Al4V. *Mater. Charact.* **75**, 79 (2013).
13. **D.R. Chichili, K.T. Ramesh, and K.J. Hemker:** Adiabatic shear localization in α -titanium: Experiments, modeling and microstructural evolution. *J. Mech. Phys. Solids* **52**, 1889 (2004).
14. **D. Rittel, P. Landau, and A. Venkert:** Dynamic recrystallization as a potential cause for adiabatic shear failure. *Phys. Rev. Lett.* **101**, 165501 (2008).
15. **Z. Zhang, D.E. Eakins, and F.P.E. Dunne:** On the formation of adiabatic shear bands in textured HCP polycrystals. *Int. J. Plast.* **79**, 196 (2016).
16. **M.A. Meyers, V.F. Nesterenko, J.C. LaSalvia, and Q. Xue:** Shear localization in dynamic deformation of materials: Microstructural evolution and self-organization. *Mater. Sci. Eng., A* **317**, 204 (2001).
17. **W-S. Lee and C-F. Lin:** High-temperature deformation behaviour of Ti6Al4V alloy evaluated by high strain-rate compression tests. *J. Mater. Process. Technol.* **75**, 127 (1998).
18. **J.W. Hutchinson and V. Tvergaard:** Shear band formation in plane strain. *Int. J. Solids Struct.* **17**, 451 (1981).
19. **D. Xing, Y.L. Bai, C. Min, and X.L. Huang:** On post-instability processes in adiabatic shear in hot rolled steel. *J. Mech. Phys. Solids* **39**, 1017 (1991).
20. **Y. Xu, Y. Bai, and M.A. Meyers:** Deformation, phase transformation and recrystallization in the shear bands induced by high-strain rate loading in titanium and its alloys. *J. Mater. Sci. Technol.* **22**, 737 (2006).
21. **S.M. Walley:** Shear localization: A historical overview. *Metall. Mater. Trans. A* **38**, 2629 (2007).
22. **S.D. Antolovich and R.W. Armstrong:** Plastic strain localization in metals: Origins and consequences. *Prog. Mater. Sci.* **59**, 1 (2014).
23. **S. Roy and S. Suwas:** On the absence of shear cracking and grain boundary cavitation in secondary tensile regions of Ti-6Al-4V-0.1B alloy during hot ($\alpha + \beta$)-compression. *Philos. Mag.* **94**, 447 (2014).
24. **A. Molinari, C. Musquar, and G. Sutter:** Adiabatic shear banding in high speed machining of Ti-6Al-4V: Experiments and modeling. *Int. J. Plast.* **18**, 443 (2002).
25. **C.S. Hong, N.R. Tao, X. Huang, and K. Lu:** Nucleation and thickening of shear bands in nano-scale twin/matrix lamellae of a Cu-Al alloy processed by dynamic plastic deformation. *Acta Mater.* **58**, 3103 (2010).
26. **T. Seshacharyulu, S.C. Medeiros, W.G. Frazier, and Y.V.R.K. Prasad:** Microstructural mechanisms during hot working of commercial grade Ti-6Al-4V with lamellar starting structure. *Mater. Sci. Eng., A* **325**, 112 (2002).
27. **X. Liu, C. Tan, J. Zhang, Y. Hu, H. Ma, F. Wang, and H. Cai:** Influence of microstructure and strain rate on adiabatic shearing behavior in Ti-6Al-4V alloys. *Mater. Sci. Eng., A* **501**, 30 (2009).
28. **R. Zhou, K.H. Pang, A. Bisht, A. Roy, S. Suwas, and V.V. Silberschmidt:** Modelling strain localization in Ti-6Al-4V at high loading rate: A phenomenological approach. *Philos. Trans. R. Soc., A* **378**, 12 (2019).
29. **S. Mironov, M. Murzinova, S. Zhrebtsov, G.A. Salishchev, and S.L. Semiatin:** Microstructure evolution during warm working of Ti-6Al-4V with a colony- α microstructure. *Acta Mater.* **57**, 2470 (2009).
30. **N.E. Paton and W.A. Backofen:** Plastic deformation of titanium at elevated temperatures. *Metall. Trans.* **1**(10), pp.2839-2847. (1970).
31. **D.L. Davidson, U.S. Lindholm, and L.M. Yeakley:** The deformation behavior of high purity polycrystalline iron and single crystal molybdenum as a function of strain rate at 300 K. *Acta Metall.* **14**, 703 (1966).
32. **F. Bachmann, R. Hielscher, P.E. Jupp, W. Pantleon, H. Schaeben, and E. Wegert:** Inferential statistics of electron backscatter diffraction data from within individual crystalline grains. *J. Appl. Crystallogr.* **43**, 1338 (2010).